Geophys. J. Int. (1995) **120,** 247–261

Shock compression and isentropic release of granite

Toshimori Sekine,* Thomas S. Duffy,† Allan M. Rubin,§ William W. Anderson and Thomas J. Ahrens

Lindhurst Laboratory of Experimental Geophysics, Seismological Laboratory 252-21, *California Institute of Technology, Pasadena,* CA 91125, *USA*

Accepted 1994 June 7. Received 1993 March 15

SUMMARY

New equation of state data for a weathered granite shocked to about 125 GPa are reported and combined with the Westerly granite data of McQueen, Marsh & Fritz (1967). The shock velocity (U_s)–particle velocity (U_p) relations can be fitted with two linear regressions: $U_s = 4.40 + 0.6U_p$ for a range of U_p up to about 2 km s^{-1} and $U_s = 2.66 + 1.49U_p$ for a range of about 2 to 5 km s^{-1}. The third-order Birch–Murnaghan equation of state parameters are $K_{os} = 51$–57 GPa and $K'_{os} = 1.4$–1.8 for the low-pressure regime and $K_{os} = 251 \pm 30$ GPa and an assumed $K'_{os} = 4$ for the high-pressure regime. Compressive waveforms in dry and water-saturated granite were measured at 10–15 GPa using the VISAR technique. The measured wave profiles were successfully modelled using a Maxwellian stress–relaxation material model. Water-saturated granite is characterized by a ~25 per cent lower yield strength and a ~75 per cent longer material relaxation time than dry granite.

From measurements of partially released states in granite, it is proposed that the high-pressure forms of tectosilicates, including granite, relax isentropically to a metastable, intermediate phase characterized by a dense (about 3.7 g cm^{-3}), highly disordered, six-fold coordinated phase which is subsequently quenched to diaplectic glasses of density ~2.3 g cm^{-3}, starting at pressure of ~10 GPa. We develop an analytical model to describe the release isentropes in the mixed-phase regime which prescribe release to a glass phase with increasing transformation to the high-pressure phase. Hugoniot and post-shock energies and temperatures derived from the release isentropes are consistent with available data and theoretical expectations for quartz and granite.

Key words: equation of state, granite, phase transitions.

INTRODUCTION

Shock Hugoniot data on silicate rocks and minerals all demonstrate major shock-induced phase transformations (e.g. see van Thiel 1977; Marsh 1980; Trunin 1986). The shock response of this class of materials is of importance in describing shock propagation from impact and explosive sources on the Earth and other planetary surfaces, as well as having applications in the study of the Earth's interior.

Granitic rocks are the most common component of the upper continental crust, and consist mainly of quartz and feldspars. The Hugoniots of tectosilicates and rocks composed chiefly of tectosilicates are all quite similar. A number of studies have been performed to measure the high-pressure properties of these minerals and their mixtures (e.g. Wackerle 1962; Ahrens, Peterson & Rosenberg 1969b; Grady, Murri & DeCarli 1975; Lyzenga, Ahrens & Mitchell 1983). The derived equation of state parameters have been compared with theoretical considerations (e.g. McQueen, Fritz & Marsh 1963; Ahrens, Anderson & Ringwood 1969a). The onset of shock-induced phase transformations usually does not occur at the thermodynamic equilibrium pressure or temperature. For example, in the case of quartz, the shock-induced high-pressure phase is inferred to be stishovite (McQueen *et al.* 1963), and this idenitfication is consistent with shock-wave recovery experiments (e.g. Milton & DeCarli 1963). For feldspars, the measured Hugoniots above 30 GPa

* Permanent address: National Institute for Research in Inorganic Materials, Tsukuba 305, Japan.
† Now at: Geophysical Laboratory, 5251 Broad Branch Rd NW, Washington, DC 20015, USA.
§ Now at: Department of Geological Sciences, Princeton University, Guyot Hall, Princeton, NJ 08544, USA.

can be interpreted in terms of a high-pressure polymorph with the hollandite structure (Ahrens *et al.* 1969a; Sekine & Ahrens 1991).

Shock-recovered samples of quartz and feldspars from above 25–30 GPa indicate transformation to diaplectic glasses, which are characterized by higher refractive indices and densities than normal fused glasses of the same composition (DeCarli & Jamieson 1959; Wackerle 1962; Kleeman 1971; Velde *et al.* 1989; Heyman & Hörz 1990). These diaplectic glasses have been intensively studied (e.g. Stöffler & Hornemann 1972). Are these diaplectic glasses characteristic of tectosilicates? Are they produced during shock compression or during isentropic release? If formation of glass occurs upon isentropic release, what is the phase present in the compressed state and at what pressure does the shocked tectosilicate transform to diaplectic glass?

Recently, isothermal compression of tectosilicates, as well as fayalite in the diamond anvil cell at room temperature, has indicated that transformation to a dense, amorphous phase occurs with an increase in the coordination of silicon and aluminium by oxygen (Hemley *et al.* 1988; Williams & Jeanloz 1989; Williams *et al.* 1990).

The purpose of this study is to present new experimental data for Hugoniot and partially released states of a weathered granite, to combine these and previous data, and to generate a complete equation of state. Initially, we summarize available data on the equation of state of granite, as well as on its major constituents, quartz and feldspar. The release adiabat states are described in terms of the third-order Birch–Murnaghan equation of state and compared with those for quartz and feldspars. We then construct analytic expressions for the release isentropes in the low-pressure, mixed-phase, and high-pressure regimes. The mixed-phase and high-pressure release isentropes are described in terms of frozen release isentropes (Grady, Murri & Fowles 1974; Swegle 1990), and, upon release to pressures in the 2 to 10 GPa range, the high-pressure phase is assumed to transform to glass, as indicated by a number of release data (Ahrens & Rosenberg 1968; Podurets, Simakov & Trunin 1976; Chhabildas & Grady 1984; Chhabildas & Miller 1985).

Experimental details

The chemical composition of the weathered granite used in the present study was determined by electron microprobe analyses of a glass formed from rock powder quenched in water. The weathered granite was melted at 1600 °C in air to obtain a homogeneous glass. Modal analysis of the weathered granite was determined by point counting. Table 1 lists the chemical composition and the mode, together with the compositions of the other granites for which equations of state have been measured (McQueen *et al.* 1967; Van Thiel 1977; Marsh 1980). The chemical compositions of all the granites are similar.

The present shock specimens were cut from a disc, 10 cm in diameter and 3 cm thick. Bulk densities ranged from 2.619 to 2.642 g cm^{-3}, while crystal densities ranged from 2.640 to 2.645 g cm^{-3}, indicating that the porosity of the samples is low. The measured longitudinal and shear sound velocities were 5.36 ± 0.10 and 3.3 ± 0.2 km s^{-1}, respectively.

Shock compression was conducted by launching impactors with the Caltech 25 mm bore, two-stage light gas gun and a 40 mm bore propellant gun. Metal-flyer-plate-bearing projectiles were used to impact the samples. The metal flyer plates were Al or Ta. In each experiment, the impact velocity of the projectile was measured by the flash X-ray method, and the shock-wave velocity was determined by measuring the traveltime of the shock wave through the sample of known thickness by means of a rotating-mirror or an image-converter streak camera. Flat and inclined mirrors were employed to observe the shock-wave traveltime (Ahrens 1987). The Hugoniot state was calculated by applying the impedance match conditions to the measured initial density, impact velocity and shock-wave velocity.

A partial or fully released state was also determined by a

Table 1. Chemical and modal compositions of several granites used for equation of state experiments.

	Composition			Mineral Content			
	Present Study(1)	Grey Granite(2)		1	2	3	4
SiO_2	73.1	71.94	Qz	41.3	19.5	28.5	21.1
TiO_2	0.15	0.26	Pl	24.8	26.5	32.5	46.7
Al_2O_3	13.9	13.68	K-fd	25.3	47.0	35.4	20.3
FeO*	1.09	4.25	Mica	8.6	5.0	3.6	4.9
MgO	0.37	0.63	Others	--	~2.5	--	7.0
CaO	0.80	2.96					
MnO	0.02	--					
K_2O	3.93	1.44					
Na_2O	4.68	2.94					
H_2O	--	1.38					
Total	98.1	99.48					

* All Fe reported as FeO.
1. Weathered granite used in the present study.
2. Grey granite from the Nevada Test Site no. 15 (van Thiel 1977).
3. Westerly granite (McQueen *et al.* 1967; Marsh 1980).
4. Biotite–chlorite granite (van Thiel 1977).

free-surface or buffer impedance mismatch observation, reduced by way of the Riemann-integral formalism (Rice, McQueen & Walsh 1958; Lyzenga *et al.* 1983). Lexan and polyethylene were used as buffer materials, mounted at the rear of the sample. Streak camera cut-offs could not always be observed for the buffer.

A velocity-sensitive interferometer (VISAR—Velocity Interferometer System for Any Reflector) (Barker & Hollenbach 1972) was employed to investigate compressive wave profiles in dry and water-saturated granite at low stresses (~10 GPa). This technique makes use of the Doppler shift of reflected laser light produced by the motion of a diffuse surface. Interference fringes proportional to the velocity of the reflector are developed in a modified Michelson interferometer and recorded using photo-multiplier tubes (Burle 7764) and digitizing oscilloscopes (HP 54111D). The VISAR used in the present experiments incorporates the push–pull modification (Hemsing 1979) for improved signal quality. The time resolution of our VISAR is estimated to be 3 ns and the velocity precision is 1 per cent. The target assembly for these experiments consisted of an aluminum driver plate (1.5 mm thick), a granite target (6.25 mm thick), a diffuse reflecting aluminum buffer (0.75 mm thick), and a LiF window (4–8 mm thick) (Fig. 1). For one shot (no. 806), the target was held in an aluminum cup and was water-saturated in vacuum. The shock

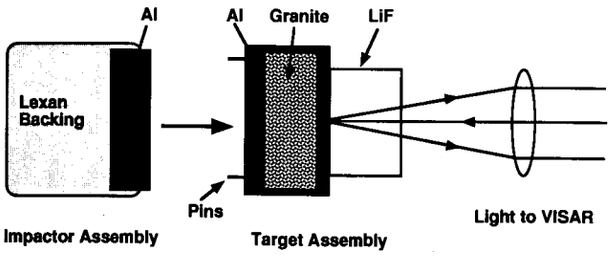

Figure 1. Experimental geometry for VISAR experiments. The impactor assembly consisted of a lexan-backed aluminum flyer plate fired at speeds of between 1.21 and 1.78 km s^{-1}. The target assembly consisted of a granite sample sandwiched between an aluminum driver and buffer. The VISAR monitors the velocity at the interface between the diffuse aluminum reflector and the LiF window.

equations of state for Al, Ta, LiF, lexan and polystyrene employed in these and the Hugoniot experiments are summarized in Table 2.

RESULTS

The results of the present experiments are given in Table 3, and are shown in Figs 2 and 3. For comparison, the Westerly granite data (McQueen *et al.* 1967) are also plotted in the figures and included in the analysis.

The shock velocity (U_s) versus particle velocity (U_p) relations shown in Fig. 2 can be characterized by two fits ($U_s = C_0 + SU_p$), with $C_0 = 4.40$ km s^{-1} and $S = 0.60$ for particle velocities up to 2.1 km s^{-1}, and $C_0 = 2.66$ km s^{-1} and $S = 1.49$ for a range of $U_p = 1.8$ to 4.8 km s^{-1}. The bulk sound velocity resulting from the measurements of V_p and V_s for dry granite at 1 atm is 3.77 ± 0.05 km s^{-1}, which is close to Westerly granite data (Marsh 1980).

However, the *P*- and *S*-wave velocities increase rapidly under confining pressure due to the closure of cracks and pores (Birch 1961). As discussed by McQueen *et al.* (1967), the extrapolation of longitudinal and shear velocities measured by Birch between 0.4 and 1.0 GPa to ambient pressure yields a longitudinal velocity of 6.04 km s^{-1} and a shear velocity of 3.47 km s^{-1}. It is expected that these values will more closely reflect the intrinsic elastic properties of granite, whereas ultrasonic velocities measured at ambient pressure will be very sensitive to the porosity of the specimen (*cf.* Table 4). The bulk sound speed, V_B, from the extrapolated Westerly data is 4.5 km s^{-1}.

Table 4 summarizes the U_s–U_p relations for various granites. Their compositions are given in Table 1. Despite their chemical variations, the U_s–U_p relations for granites are all similar. C_0 ranges between 2.10 and 2.66 km s^{-1} and S is between 1.49 and 1.63, when U_p ranges from 1.8 to 6 km s^{-1}. Above $U_p = 5$ km s^{-1}, only a few data are available (biotite–chlorite granite and Soviet granite), and Trunin *et al.* (1988) obtained a linear relation for the Soviet granite (Table 4).

Telegin *et al.* (1980) have demonstrated good agreement between the observed Hugoniot and the calculated Hugoniot based upon the oxide-mixture model. According

Table 2. Equation of state and constitutive parameters used in the present study.

Material	Initial Density (g/cm^3)	C_0 (km/sec)	S	ν	Y_0 (GPa)	Ref.
Granite (dry)	2.62	4.40	0.60	0.24	3.6	3
Granite (wet)	2.62	4.40	0.60	0.24	2.7	3
Al 2024	2.785	5.328	1.338	0.34	0.3	1
Ta	16.656	3.43	1.19	-	-	2
LiF	2.638	5.15	1.35	-	-	1
Lexan	1.193	2.449	1.498	-	-	1
Polystyrene foam	0.055	0.243	1.118	-	-	1

References.
1. Marsh (1980).
2. McQueen *et al.* (1970).
3. This study.

Table 3. Experimental results for granite.

				Hugoniot State				Partial Release State			
Shot #	Flyer/Driver	Impact Velocity (km/sec)	Initial Density (g/cm^3)	Shock Velocity (km/sec)	Particle Velocity (km/sec)	Pressure (GPa)	Density (g/cm^3)	Shock Velocity (km/sec)	Particle Velocity (km/sec)	Pressure (GPa)	Density (g/cm^3)
				VISAR Experiments							
805	Al	1.21 ±0.01	2.630 ±0.002	plastic 4.64 ±0.2	0.69 ±0.02	8.5 ±0.5	3.09 ±0.04				
806 (wet)	Al	1.43 ±0.01	2.619 ±0.002	plastic 4.88 ±0.2	0.78 ±0.02	9.9 ±0.6	3.11 ±0.04				
803	Al	1.78 ±0.01	2.628 ±0.002	plastic 4.88 ±0.2	1.03 ±0.01	13.2 ±0.5	3.333 ±0.03				
				Streak Camera Experiments							
832	Al	2.21 ±0.01	2.633 ±0.001	elastic 5.87 ±0.14	0.575 0.045	8.9 ±1.6	2.919 ±0.102				
				plastic 5.38 ±0.10	1.86 ±0.09	27.1 ±2.5	3.985 ±0.218	lexan 5.00 ±0.12	1.78 ±0.08	10.2 ±0.7	3.960 ±0.046
								postshock ---	3.799 ±0.166	0	2.566 ±0.046
827	Ta	2.465 ±0.010	2.642 ±0.002	plastic 5.73 ±0.05	2.01 ±0.01	30.4 ±0.3	4.066 ±0.024	lexan 5.45 ±0.06	2.00 ±0.04	13.0 ±0.4	4.065 ±0.118
222	Al	4.54 ±0.005	2.624 ±0.002	plastic 6.64 ±0.10	2.53 ±0.03	44.1 ±0.7	4.238 ±0.063				
240[a]	Al	4.524 ±0.003	2.622 ±0.001	plastic 6.61 ±0.08	2.54 ±0.04	44.1 ±0.1	4.259 ±0.050	lexan 6.82 ±.23	2.92 ±.17	23.7 ±.2.2	4.139 ±.094
237[a]	Al	5.225 ±0.003	2.619 ±0.002	plastic 6.78 ±0.14	2.96 ±0.10	52.6 ±2.1	4.652 ±0.097	lexan 7.28 ±.44	3.65 ±.34	31.7 ±.5.1	4.214 ±.117
229	Al	5.31 ±0.05	2.638 ±0.002	plastic 6.92 ±0.10	2.97 ±0.04	54.1 ±0.9	4.608 ±0.096				
236	Al	5.379 ±0.003	2.620 ±0.001	plastic 7.21 ±0.11	2.99 ±0.08	56.6 ±1.8	4.479 ±0.066				
230	Ta	4.09 ±0.04	2.638 ±0.002	plastic 7.52 ±0.05	3.23 ±0.03	64.0 ±0.7	4.621 ±0.045				
220	Ta	6.22 ±0.06	2.625 ±0.002	plastic 9.89 ±0.03	4.77 ±0.05	124.0 ±1.3	5.075 ±0.052	lexan 10.22 ±0.052	5.91 ±0.10	72.0 ±0.08	4.512 ±0.127

[a] Release points not plotted in Fig. 8 for clarity.

to this model,

$$C_0 = a_0 + a_1\rho_0 + \sum_i a_i Z_i, \tag{1a}$$

$$S = b_0 + b_1\rho_0 + \sum_i b_i Z_i, \tag{1b}$$

where ρ_0 is the initial density, Z_i is the weight percentage of component oxide i, and a_0, a_1, a_i, b_0, b_1 and b_i are constants. The constants reported by Telegin *et al.* (1980) are used in the present calculations. The calculations are restricted to the high-pressure phase region. The results shown in Fig. 2 (dotted curve) ($U_s = 2.369 + 1.59U_p$ km s^{-1}) demonstrate a good approximation to the Hugoniot data in the high-pressure regime.

We also apply a mineral-mixture model (Al'tshuler & Sharipdzhanov 1971) to obtain a theoretical Hugoniot for the present weathered granite. In this model,

$$V(P) = \sum_i V_i(P) M_i, \tag{2}$$

where V_i is the volume of constituent mineral i at pressure P and M_i is the mass fraction of mineral i. Using the Rankine–Hugoniot equations, U_s and U_p are computed from the resulting P–V relation. The granite is taken to be a mineral mixture consisting of the modal composition (Table 1). The Hugoniots for plagioclase and K-feldspar have been recognized to be insensitive to composition, and the microcline Hugoniot (Ahrens *et al.* 1969b; Simakov *et al.* 1974) was used in the present calculation. The quartz Hugoniot was taken from the data of Wackerle (1962) and Trunin *et al.* (1970). The muscovite Hugoniot, which has recently been determined (Sekine, Rubin & Ahrens 1991),

stress of 3.1 GPa from wave profile measurements on dry granite.

The same precursor velocity was used in the models for both dry and wet granite, indicating that elastic velocity is not significantly affected by water saturation at these pressures. The value of V_p of granite increases under H_2O-saturated conditions (Nur & Simmons 1969). It would seem that the presence of water in granite has a critical influence only in the relatively low-pressure regime ($P \leq 0.1$ GPa). It appears that the small amount of water that can be injected in the granite's pores has little effect on wave velocity in the range of the present experiments. This is consistent with other studies on wet, low-porosity rocks.

The precursor velocity used to fit the VISAR experiments is consistent with ultrasonic data and the inclined-mirror experiment. The equation of state used to fit the wave profiles is shown as the solid line in Fig. 2, and it agrees with the determinations from the elastic–plastic wave separations. The low-pressure-phase data lie slightly below the Westerly granite data of McQueen *et al.* (1967) and this may reflect compositional differences. For all experiments, unloading begins well before the time predicted by the wavecode models. This is due to the arrival of edge effects prior to unloading from the rear of the flyer.

The measured release states of the present granite are shown in Fig. 3, together with the data of Swegle (1990). The release of shocked granite from about 26–30 GPa Hugoniot pressures was found to occur along pressure–density paths characteristic of the high-pressure phase(s). At lower pressures, the final unloading states were generally close to the low-pressure-phase initial density. Swegle (1989) also observed that the unloading data of granite from 27 GPa demonstrated initial unloading characteristic of the high-pressure phase. Swegle's (1990) data indicate that the reverse transition is not initiated immediately upon unloading. This behaviour can be seen at least up to the Hugoniot pressure of 54 GPa for granite (Swegle 1990). However, the release path observed from one datum at the Hugoniot pressure of 124 GPa indicates a shallower slope than the Hugoniot. Swegle (1989) provides a similar unloading profile for granite at 92 GPa.

DISCUSSION

The shock-wave data are used to obtain equation of state parameters K_{os} (the zero-pressure adiabatic bulk modulus) and K'_{os} (its first pressure derivative) from the third-order Eulerian finite-strain (Birch–Murnaghan) equation of state for granite. We use the approach of Ahrens & Jeanloz (1987) and Heinz & Jeanloz (1984) to analyse the Hugoniot data.

The Eulerian strain f is expressed as

$$f = \frac{1}{2}\left[\left(\frac{V_0}{V}\right)^{2/3} - 1\right], \tag{3}$$

where V and V_0 are the Hugoniot and ambient volumes of the sample, respectively. The normalized pressure F'_{HS} is given by

$$F'_{HS} = F_{HS} + \Delta F_{tr} = K_{os}(1 - 2\xi_s f_{3H} + \cdots), \tag{4}$$

where

$$F_{HS} = \frac{1 - \gamma/[(1+2f)^{3/2} - 1]/2}{3f(1+2f)^{3/2}[1 + (2 - 1.5\gamma)f]} P_H, \tag{5}$$

$$\Delta F_{tr} = \frac{\rho_0 \gamma E_{tr}}{3f[1 + (2 - 1.5\gamma)f]}, \tag{6}$$

$$f_{3H} = \frac{f[1 + (2 - \gamma)f]}{1 + (2 - 1.5\gamma)f} \tag{7}$$

and

$$\xi_s = 3(4 - K'_{os})/4, \tag{8}$$

where P_H is the Hugoniot pressure.

The parameters F_{HS}, f_{3H}, and ΔF_{tr} are obtained from the experimental data, and the parameters K_{os} and K'_{os} are obtained from a linear fit to eq. (4). γ is calculated according to the following equations:

$$\gamma = \gamma_0\left(\frac{V}{V_0}\right)^q \tag{9}$$

and

$$\gamma_0 = \frac{\alpha K_{os}}{\rho_0 C_p}, \tag{10}$$

where α is the volume coefficient of thermal expansion, C_p is the specific heat at constant pressure, and q is a free parameter. Errors in F'_{HS} and f_{3H} are estimated by standard error propagation techniques using the expressions in Ahrens & Jeanloz (1987).

Low-pressure regime

For granite in the low-pressure regime ($P < 20$ GPa), $E_{tr} = 0$, $\rho_0 = 2.63$ g cm^{-3}, $\gamma_0 = 1.0 \pm 0.5$, and $q = 1.0 \pm 1.0$ were used in the present computation. These values cover reasonable ranges for γ_0 and q, and the resulting K_{os} and K'_{os} are not strongly sensitive to the values of γ_0 and q used. An unweighted linear least-squares fit to the experimental data of McQueen *et al.* (1967) below a shock pressure of 20 GPa yields $K_{os} = 57$ GPa and $K'_{os} = 1.8$. A zero-order fit ($K'_{os} = 4$) of the experimental data yields $K_{os} = 40$ GPa. Ultrasonic determinations of K_{os} give 37 GPa, which is close to the value of K_{os} of quartz, while the extrapolated value from the data of Birch (1961) is 53 GPa. The Hugoniot fit to the VISAR data yields $K_{os} = 51$ GPa and $K'_{os} = 1.4$.

The bulk moduli for end-member feldspars range between 67 and 106 GPa (Angel *et al.* 1988). The value of $K_{os} = 51$–57 GPa for granite is consistent with a mixture of quartz and feldspars. However, some of the deformational Hugoniot points below 20 GPa may be mixed-phase states. The equations of state are summarized in Table 5.

High-pressure regime

Equation of state parameters are calculated for granite in the high-pressure regime ($P > 39$ GPa) in the same manner as for the low-pressure regime. The values of γ_0 and q are not well constrained, however. E_{tr} is estimated to be

Table 4. A comparison of equations of state for granites.

No.	Co (km/s)	S	Initial Density (g/cm^3)	U_p Range (km/s)	V_p (km/s)	V_S (km/s)
1	4.40	0.60	2.630	0-2.1	5.36±0.10	3.3±0.2
	2.66	1.49		1.8-4.8		
2	2.52	1.50	2.67	2-4	5.64	3.53
3	2.10	1.63	2.62	2.1-4	5.33	3.28
	2.59	1.51	2.62	1.8-4		
4	2.22	1.63	2.68	3-6		
5	2.435	1.525	2.60	2.16-5.10		
	3.75	1.28	2.60	5.10-8.9		

Notes. Granites nos. 1 to 4 correspond to the number in Table 1. Granite No. 5 is from Trunin *et al.* (1988).

included in the model. In this case, the deviatoric stresses are obtained from a relation of the form

$$\frac{\partial \sigma^{\mathrm{d}}}{\partial t} = 2G\left(\frac{\partial \varepsilon}{\partial t} - g\right),$$

where σ^{d} is the deviatoric stress, G is the shear modulus, ε is the strain, t is the time, and g is a relaxation function. The relaxation function, g, is simply given by

$$g = \frac{\sigma^{\mathrm{d}} - \sigma_{\mathrm{e}}^{\mathrm{d}}}{Gt_{\mathrm{r}}}$$

where $\sigma_{\mathrm{e}}^{\mathrm{d}}$ is the equilibrium stress deviator, and t_{r} is the material relaxation time. The predicted waveforms are in very good agreement with the experimental data (Fig. 4). The main differences between the model and data are in the elastic portion, where the data is significantly more dispersive than the model prediction.

There are significant differences in the compressive behaviour of dry and water-saturated granite. The dry experiments were fitted using a yield stress of 3.6 GPa and a relaxation time of 20 ns. The wet experiment, however, required a lower yield stress (2.7 GPa) and a longer relaxation time (35 ns). The lower compressive strength of the wet sample could be due to the presence of water along cracks, reducing the effective normal stress and therefore the frictional strength of the flaws, thus promoting brittle failure. Furthermore, the longer relaxation time of the water-saturated sample may reflect an increase in viscosity due to the presence of fluid. Swegle (1989) reported a yield

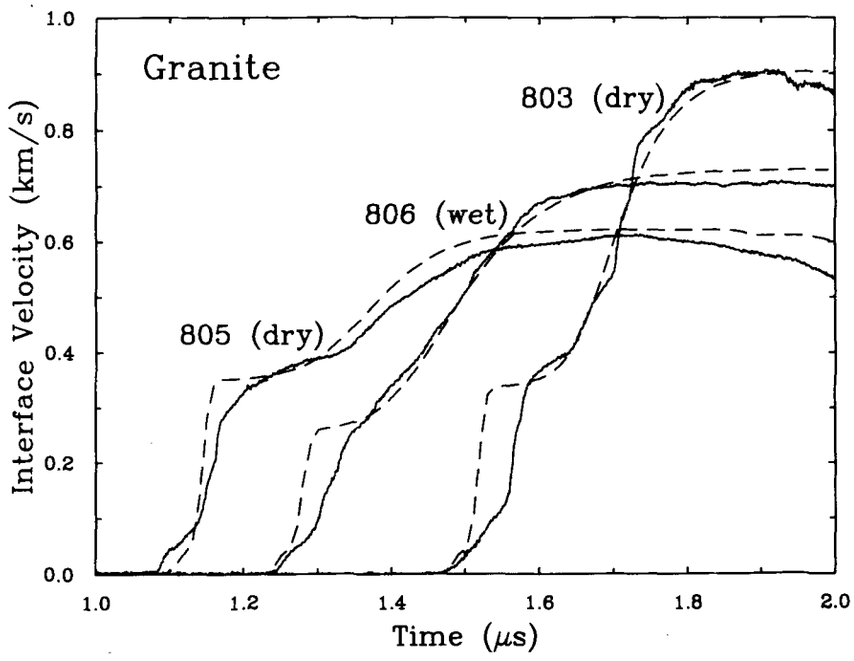

Figure 4. Interface compressive wave profiles in dry and water-saturated granite. Solid curves are experimental data and dashed curves are WONDY simulations. Shot 803 was scaled by a factor of 1.12 to account for optical misalignment of the VISAR. The times are arbitrary. Granite was modelled as a Maxwellian elastic–stress-relaxing solid. Initial response is assumed to be elastic, although measured profiles show significant dispersion. The water-saturated sample is characterized by a longer relaxation time constant and lower yield stress.

Then the final image matrix $\mathbf{D}(f, t)$ of detectable signal energy is composed by

$$\mathbf{D}(f,t) = \begin{cases} \log_2[\mathbf{A}(f,t) - 2^{M(f)}] & \text{if eq. (4) holds} \\ \text{“}-\text{”} & \text{otherwise} \end{cases} \quad (5)$$

where everything below the threshold is blanked as 'non-significant' and will be marked by a symbolic minus sign " − ". Taking signal and noise as uncorrelated, we could correct for the noise offset by subtracting the median of its energy. The whole calculation preserves the relative energy ratios within the seismogram as we demanded for the subsequent pattern adaptation. Related to $\mathbf{D}(f, t)$, we also need the vector $N_D(f)$ which describes the log-noise variance in the actual data. It is defined by

$$N_D(f) = \log_2[2^{M(f)+S(f)} - 2^{M(f)}]. \quad (6)$$

Finally $\mathbf{D}(f, t)$ and $N_D(f)$ can be rounded to nearest integers. This will suppress any fine-grain amplitude differences $< \pm\sqrt{2}$ as we chose the log base of 2 for the energy in eq. (2). Only for the steps of correlation and display, the sonogram is equalized to an all-positive matrix by

$$\mathbf{D}^+(f,t) = \mathbf{D}(f,t) - [N_D(f) - 1] \quad \text{for} \quad \mathbf{D}(f,t) \neq \text{“}-\text{”}, \quad (7)$$

which performs similar to a pre-whitening filter in traditional detector theory.

Pattern definition

In PR, we require the explicit definition of desired signal patterns. Fortunately matrix $\mathbf{D}(f, t)$ of any single seismic event can already be taken as pattern $\mathbf{P}(f, t)$ because of the chosen technique of pattern adaptation. The only constraints are: (1) the selection of a sufficiently large event for a good S/N ratio and (2) the definition of an 'inverse area' of symbolic minus signs before the P onset. (Additionally, areas of weak signal energy can be excluded from the calculation by zeroing.) In the final calculation of pattern fit, the inverse area will result in a horizontal edge sharpening to significantly enhance the onset timing. However, even the most exact onset times of sonogram detection obviously carry the principal uncertainty of half a FFT window length [i.e. one sample of image matrix $\mathbf{D}(f, t)$].

Pattern adaptation

As described by Fig. 3, adapting a given pattern to the actual S/N ratio is a two-step approach. The first step performs amplitude adjustment based on the median of some reference samples that should mark an area of stable energy. The adjustment is defined by

$$\begin{aligned} \mathbf{P}'(f,t) &= \mathbf{P}(f,t) - (P_{\text{ref}} - D_{\text{ref}}) \quad \text{for} \quad \mathbf{P}(f,t) \neq \text{“}-\text{”} \\ N'_P(f) &= N_P(f) - (P_{\text{ref}} - D_{\text{ref}}) \end{aligned} \quad (8)$$

for the pattern and its associated noise vector.

Once both matrices are in the same range of amplitudes, the second prerequisite for a comparison is to harmonize their noise levels. This is achieved by transposing the noise variance $N_D(f)$ of the data onto the pattern by

$$N''_P(f) = N_D(f). \quad (9)$$

Obviously, this will also affect the detectability of pattern energy. While the dominant features stay above the new noise threshold to remain valid, some weaker details of the PSD image get modified by the two *masking criteria* (note: eq. 10 is not applied to the inverse area before the P onset)

$$\begin{aligned} &(1)\ \text{if} \quad [\mathbf{P}'(f,t) \neq 0 \quad \text{and} \ \mathbf{P}'(f,t) < N_D(f)] \quad \mathbf{P}''(f,t) = \text{“}-\text{”} \\ &(2)\ \text{else if} \ [\mathbf{P}(f,t) = \text{“}-\text{”} \ \text{and} \ \mathbf{D}(f,t) < N'_P(f)] \quad \mathbf{P}''(f,t) = 0 \\ &\quad \text{else} \qquad\qquad\qquad\qquad\qquad\qquad\qquad\quad \mathbf{P}''(f,t) = \mathbf{P}'(f,t). \end{aligned} \quad (10)$$

The first criterion tests if the down-scaled pattern energy can still be detected in the actual noise. If this condition fails, we demand the prediction of *no energy* for $\mathbf{P}''(f, t)$. The second criterion looks for those (few) samples of actual energy in $\mathbf{D}(f, t)$ that could fall below the inherent noise of $\mathbf{P}''(f, t)$ after being shifted in eq. (8). The significance of these samples is unknown in the subsequent recognition process. To ignore these we mark them in $\mathbf{P}''(f, t)$ by zero. Altogether, $\mathbf{P}''(f, t)$ represents that fraction of $\mathbf{P}'(f, t)$ that remains detectable in the actual ratio of signal amplitudes and noise conditions.

Pattern recognition

The calculation of the pattern fit 'fit(t)' is based on the pre-whitened matrices $\mathbf{D}^+(f, t)$ of eq. (7) and $\mathbf{P}^+(f, t)$ defined by

$$\mathbf{P}^+(f,t) = \mathbf{P}''(f,t) - [N''_P(f) - 1]. \quad (11)$$

Consequently, this is an evaluation of the whole image and not only of maximum amplitudes. Prior to this final matrix comparison, the areas of $\mathbf{D}^+(f, t)$ and $\mathbf{P}^+(f, t)$ that display *no energy* by our formal " − " must be set to actual values. In principle we are free to choose any value, but it's a good idea to demand fit(t) = 0 per frequency band if either $\mathbf{D}^+(f, t)$ or $\mathbf{P}^+(f, t)$ consists of random noise. According to this effect, we call these restrictions 'balance conditions'. So the symbolic minus signs in $\mathbf{D}^+(f, t)$ are modified to

$$ms_D(f) = -\frac{25\%}{100\% - 25\%} = -\frac{1}{3} \quad (12)$$

where the percentage values represent the chosen fractiles in the detection threshold of eq. (4). The result gets independent of frequency because of our prior pre-whitening. Likewise the symbolic minus signs in $\mathbf{P}^+(f, t)$ are transformed to

$$ms_P(f) = -\frac{\sum_\tau \mathbf{P}^+(f,\tau)}{n_-(f)} \quad (13)$$

where $n_-(f)$ is the number of minus signs per frequency band; the sum over $\mathbf{P}^+(f, \tau)$ must only be performed on positive values.

The comparison between pattern and data resembles a cross-correlation, i.e.

$$\text{fit}(t + t_0) = \frac{\sum_{f,\tau} \mathbf{D}^+(f, t+\tau)\mathbf{P}^+(f,\tau)}{0.5[\sum_{f,\tau} \mathbf{D}^+(f, t+\tau)^2 + \sum_{f,\tau} \mathbf{P}^+(f,\tau)^2]}. \quad (14)$$

The correlation starts at offset time t, but to achieve the true

Table 5. Summary of equation of state parameters of granite (Gra), quartz (Qz), and Feldspar (Fld) for the low-pressure regime (LP) and high-pressure regime (HP).

	Gra				Qz [2]				Fld [3]	
	LP	HP	LP	HP	LP	HP	LP	HP	LP	HP
ρ_0 (g/cm^3)	2.63	4.02 [1]	2.65	4.19	2.65	4.29	2.65	4.287	2.65	3.75
K_{os} (GPa)	51-57	251	37.7	350	37.7	306	37.7	350	80	200
K'_{os}	1.4-1.8	4.0	6.4	3.3	7.0	5.4	6.4	3.3	4.0	2.3
E_{tr} (kJ/g)	----	0.8			----	0.82	----		----	0.5
Ref.	1		2		3		2		4	5

Notes. [1] Obtained as a mixture of 50 per cent stishovite and 50 per cent high-presure feldspar with the hollandite structure.
[2] Quartz transforms to stishovite.
[3] Feldspar transforms to the hollandite form.
References 1–present study, 2–Swegle (1990), 3–Lyzenga *et al.* (1983) and Tan & Ahrens (1990), 4–Angel *et al.* (1988), and 5–Sekine & Ahrens (1992).

0.8 ± 0.5 kJ g^{-1} based on the transition energies of quartz to stishovite, and of feldspars to the hollandite structures. Although the transition energy varies with feldspar composition, the stated error range for E_{tr} covers the whole range of variation of feldspar composition. The zero-pressure density of the granite in the high-pressure regime is calculated to be 4.02 g cm^{-3} from stishovite and hollandite densities. The hollandite density varies also with the initial feldspar composition, and was approximated by the modal composition. We assumed that $\gamma_0 = 1.0 \pm 0.5$ and $q = 1.0 \pm 1.0$. A weighted least-squares fit to the data yields $K_{os} = 325 \pm 50$ GPa and $K'_{os} = 1.3 \pm 1.9$. If the pressure derivative of the bulk modulus is assumed to be 4, a bulk modulus of 251 ± 30 GPa is obtained. Fits to the data in the F_{HS}–f_{3H} plane are shown in Fig. 5. The data of shot numbers 222 and 240 were excluded from the analysis because of errors in F_{HS} that were 2 times greater than the remaining data. The high-pressure-phase parameters for granite are comparable to those obtained for quartz (Table 5), although there are differences in the assumed Grüneisen parameter and its volume dependence for the two materials. Swegle (1990) gave the same bulk modulus and pressure derivative for quartz and granite in both the low-pressure and high-pressure regimes. They are compared in Table 5. Recent analyses of Hugoniot data for various feldspars provide ranges of K_{os} and K'_{os} as well as the zero-pressure densities, based on shocked feldspars possessing the hollandite structure (Sekine & Ahrens 1992). The equation of state parameters for granite are between those of quartz and feldspars for both the low- and high-pressure regimes.

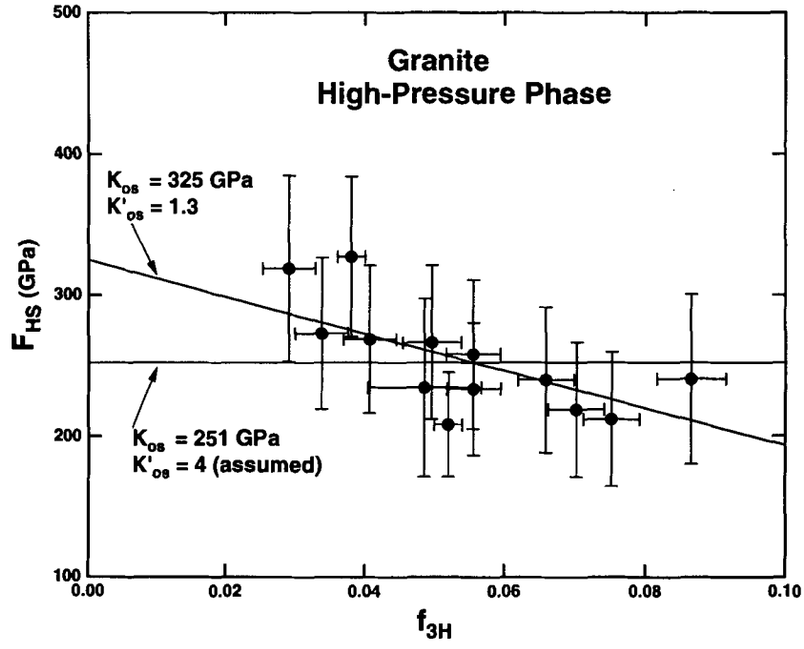

Figure 5. Shock-wave data for the high-pressure phases of granite displayed in terms of normalized pressure versus normalized strain. The symbols represent the data of this study and Marsh (1980) for $P > 39$ GPa, with the exception of shot no. 222. The error bars reflect uncertainties in the density of the high-pressure phase, the Grüneisen parameter and its volume dependence, and the transition energy, but not the uncertainty of the individual pressure–density points. The parameters of two possible fits to the data are indicated.

Release states

The Hugoniots and equation of state parameters for quartz, eldspars and granite are quite similar, as summarized in 'able 5. The release adiabat states measured for shocked uartz (Podurets *et al.* 1976; Chhabildas & Miller 1985), eldspars (Ahrens *et al.* 1969b; Grady & Murri 1976) and ranite (Swegle 1989, 1990) also show similar release paths, epending mainly upon the initial shock state. These release diabats have been measured by independent methods: the npedance mismatch buffer method (Ahrens *et al.* 1969; 'odurets *et al.* 1976), the manganin transducer record Grady & Murri 1976) and the velocity interferometer VISAR) method (Chhabildas & Miller 1985; Swegle 1989).

Because quartz has been studied widely under dynamic onditions and shows similar behaviour to granite, we begin ur analysis with a detailed examination of the release ehaviour of quartz. Fig. 6 shows the release adiabats easured for quartz. The release adiabats from shocked uartz in the mixed-phase regime are approximated by nloading paths in which the quantity of low- and igh-pressure phase in the mixture is frozen at pressures own to about 8 GPa (Grady *et al.* 1974; Swegle 1989). At his point, the volumes expand to the initial volume with urther decreasing pressure.

The release adiabats from the stishovite regime, however, eem to occur along paths leading to less dense ero-pressure material than the zero-pressure density of the igh-pressure form (stishovite), especially when the release ressure reaches within the mixed-phase regime. It appears that a material with a specific volume of about 0.270 $cm^3 g^{-1}$ is produced during the unloading process, and may then revert to a diaplectic glass on further pressure release to ambient pressure and temperature, as observed in the shock-recovery experiments on quartz. This apparent density, in fact, may be due to the formation of a diaplectic glass with six-fold coordinated silicon with oxygen. We set the post-shock quartz specific volume to be 0.44 $cm^3 g^{-1}$, a density proposed by Stöffler & Hornemann (1972). Chhabildas & Miller (1985) suggest that material of this density might represent a high-density quartz liquid produced above the melting point during unloading.

Figure 7 displays calculations of release adiabats in the mixed-phase regime, based on the mixing of Hugoniots for the quartz reigme and the stishovite regime, for a range of pressures. In this model, the mass fraction of stishovite is frozen in the mixed phase during the release state until the pressure drops down to a critical a value represented by the relation P (GPa) = 32.2–85.5 V ($cm^3 g^{-1}$) shown in Fig. 7. The reverse transformation is likely to be thermally controlled. Huffman *et al.* (1993) have recently discussed kinetic effects in the shock response of quartz. The above equation is chosen to match both the release isentrope data and the post-shock densities measured by Stöffler & Hornemann (1972). Further release causes the formation of

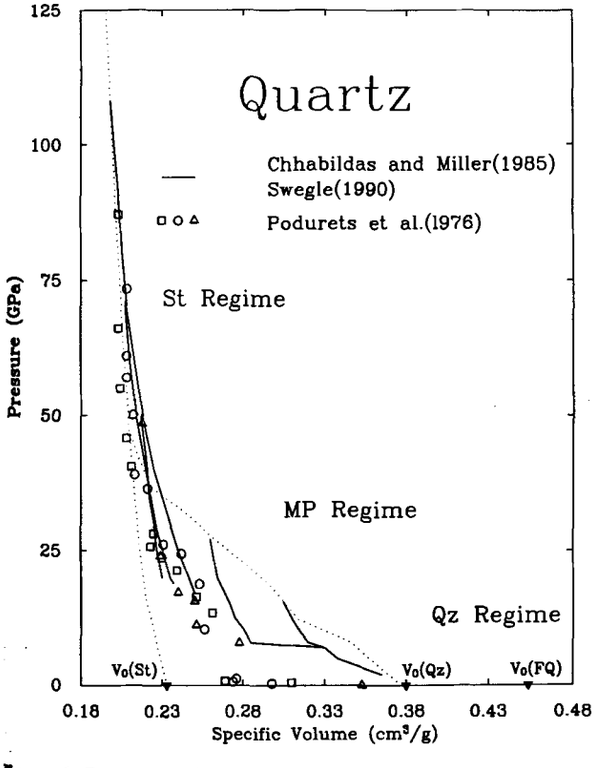

Figure 6. Pressure–volume relations for quartz release paths. Data rom Podurets *et al.* (1976), Chhabildas & Miller (1985) and Swegle 1990). St: stishovite; MP: mixed phase; Qtz: quartz; FQ: fused uartz.

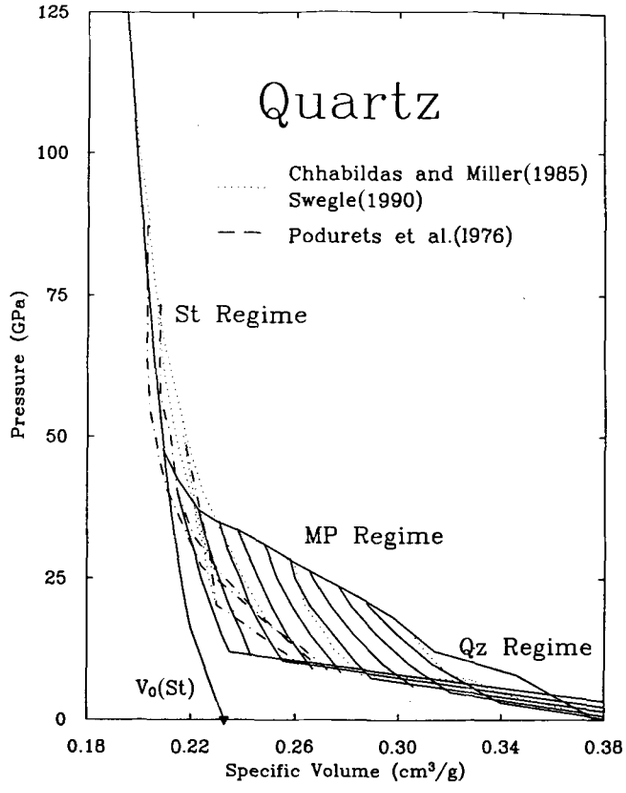

Figure 7. Pressure–volume relations for quartz release paths. Dotted and broken curves illustrate experimental data, and solid curves illustrate Hugoniot curves and calculated release paths. Solid curves are computed based on mixed Hugoniots of quartz and stishovite regimes, with mass fractions at 0.1 intervals for stishovite. Below critical pressures (Table 6), the release paths are modelled by straight lines. The zero-pressure volume of post-shock quartz shocked above some 50 GPa was taken to be 0.44 $cm^3 g^{-1}$.

Table 6. Summary of equation of state parameters of model release adiabats for quartz.

Mass Fraction		Hugoniot State				Birch Murnaghan Relations for Frozen Release Isentrope			Critical Pressure	Final Density	Release State	
LP	HP	P_H (GPa)	V_H (cm^3/g)	E_H (J/g)	T_H (K)	ρ_0(g/cm^3)	K_{os}(GPa)	K'_{os}	P_c(GPa)	ρ_0(g/cm^3)	E_R (J/g)	T_R (K)
1.0	0.0					2.65	88[1)]	6.4[1)]	–	--	--	--
0.9	0.1	20.5	.288	912	792	2.75	37	7.9	3.1	2.61	616	614
0.8	0.2	23.5	.277	1175	1017	2.87	42	8.3	5.0	2.56	721	753
0.7	0.3	26	.266	1443	1232	2.99	47	8.1	6.0	2.53	844	874
0.6	0.4	28.5	.258	1696	1502	3.13	47	10.7	7.4	2.49	928	1022
0.5	0.5	31	.248	2000	1768	3.28	59	10.1	8.4	2.44	1086	1148
0.4	0.6	33.5	.238	2328	1982	3.44	72	9.3	9.0	2.41	1232	1301
0.3	0.7	35	.231	2555	2265	3.62	93	8.7	10.5	2.38	1373	1373
0.2	0.8	37	.223	2849	2583	3.82	112	9.9	11.4	2.34	1509	1502
0.1	0.9	40	.215	3240	2995	4.05	213	4.3	12.0	2.30	1687	1673
0.0	1.0					4.29	316[1)]	4.0*	12*	2.27*		

* Assumed values.
[1] Sumino & Anderson (1984).

diaplectic glass and the final volume of post-shock quartz is given by the relation V (cm^3 g^{-1}) $= 0.063M + 0.377$ at ambient conditions, where M is the mass fraction of stishovite at the Hugoniot state, as listed in Table 6. This model calculation is compared with the experimental data (Podurets *et al.* 1976; Chhabildas & Miller 1985; Swegle 1990). The calculated unloading curves in the mixed-phase region were used to obtain Birch–Murnaghan parameters for the release curves (Table 6). The zero-pressure densities were taken from the relative mass fraction of quartz ($\rho_0 = 2.65$ g cm^{-3}) and stishovite ($\rho_0 = 4.29$ g cm^{-3}). The bulk modulus increases with increasing stishovite fraction, whereas the pressure derivative of the bulk modulus ranges from 8 to 10. Ultrasonic values for quartz and stishovite are also listed in Table 6. Unloading from higher pressures in the stishovite regime leads to a lower apparent density of the high-pressure phase, as discussed above. This is consistent with initial transformation to stishovite followed by formation of glass at higher stresses (Kleeman & Ahrens 1973). For release paths from the stishovite Hugoniot regime at 71 and 108 GPa, the zero-pressure density of 3.7 g cm^{-3}, $\gamma_0 = 1.0$ and $q = 1.0$ were taken to obtain the equation of state parameters. The fit yields $K_{os} = 65$–69 GPa and $K'_{os} = 6$–9.

As seen in Fig. 3, the release path of granite from 30 GPa also appears to behave in a similar manner to that proposed for quartz. Fig. 8 compares the calculated release paths of granite in the mixed-phase regime with the experimental data. The calculations are based on the mixing of the two Hugoniots for the low-pressure ($\rho_0 = 2.63$ g cm^{-3}) and high-pressure ($\rho_0 = 4.03$ g cm^{-3}) regimes and the frozen mass fraction of the Hugoniot state, down to a critical pressure. Below the critical pressure, given by P(GPa) = 29.1–77.2 V (cm^{-3} g^{-1}), the release paths are represented by straight lines on which the formation of diaplectic glasses proceeds.

By applying the finite-strain formalism to parts of the release adiabats as above, we obtain K_{os} and K'_{os} for granite. The results are listed in Table 7, together with the zero-pressure density of granite, the critical pressure and final density for the release paths, and the zero-pressure density of post-shock granite. We assumed the same density

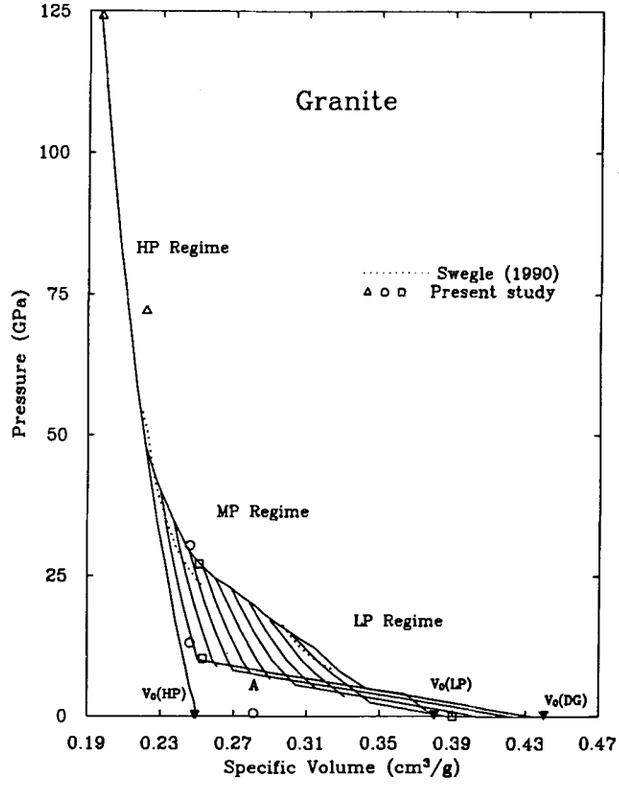

Figure 8. Comparison of pressure–volume relations for measured granite release paths with the model calculations. HP: high pressure; LP: low pressure; MP: mixed phase; DG: diaplectic glass.

of 2.27 g cm^{-3} as in quartz for the proposed diaplectic glass of granite (Stöffler & Hornemann 1972). The unloading paths below the critical pressure are associated with relatively large volume changes (Fig. 8). The critical pressure (and density) may vary with the pressure of the Hugoniot state (Chhabildas & Miller 1985). K_{os} and K'_{os} along the release paths for granite are similar to quartz values. At higher pressure, the unloading behaviour is distinctly different and proceeds to a final density of

Table 7. Summary of equation of state parameters of model release adiabats for granite.

Mass fraction		Hugoniot State				Birch-Murnaghan relations for frozen release isentrope			Critical pressure	Final density	Release State	
LP	HP	P_H (GPa)	V_H (cm^3/g)	E_H (J/gm)	T_H (K)	ρ_o(g/m^3)	K_{os}(GPa)	K'_{os}	P_c(GPa)	ρ_{oo}(g/cm^3)	E_R (J/gm)	T_R (K)
1.0	0.0					2.63						
0.9	0.1	14.5	.302	566	615	2.72	31	10.3	2.4	2.59	395	492
0.8	0.2	17	.290	765	763	2.83	44	7.3	3.5	2.55	497	587
0.7	0.3	20	.279	1012	955	2.93	45	8.1	5.0	2.51	622	697
0.6	0.4	22.5	.269	1249	1152	3.05	55	7.7	5.6	2.48	725	811
0.5	0.5	24.5	.260	1470	1326	3.18	58	9.5	6.6	2.44	845	896
0.4	0.6	26.5	.253	1683	1545	3.32	73	9.4	7.4	2.40	937	1003
0.3	0.7	30	.245	2022	1886	3.47	90	9.8	8.1	2.37	1063	1186
0.2	0.8	35	.237	2501	2417	3.64	133	8.1	8.8	2.34	1206	1465
0.1	0.9	40	.230	3004	2943	3.82	189	8.0	10.0	2.30	1400	1713
0	1.0					4.02*			10*	2.27*		

* Assumed values.

3.7 g cm^{-3}. The Birch–Murnaghan parameters are also very different. By fitting to the unloading path from 54 GPa (Swegle 1989), we obtain $K_{os} = 205$ GPa and $K'_{os} = 0.56$.

According to Swegle (1989), the unloading processes of granite differ from those of quartz. In crystalline quartz, the reverse transformation is well described by the equilibrium reverse transition and by frozen phases until the equilibrium phase boundary is reached, and then the material reverts to the initial phase. This behaviour is also the case for fine-grained polycrystalline quartz (Grady *et al.* 1974). In the unloading paths of granite, no part is described by the equilibrium reverse transition, although they are characterized by frozen high- and low-pressure phases. The unloading paths of feldspars (Ahrens *et al.* 1969; Grady & Murri 1976) illustrate a different behaviour from that of quartz, showing a deviation from the frozen high- and low-pressure-phase mixtures towards low density, well above the expected equilibrium boundary for the high-pressure phase (hollandite).

The conditions for formation of diaplectic glasses appear to be restricted to only part of the high-pressure phase present in the Hugoniot state, which reverts to a disordered diaplectic glass via solid–solid transition. Shock-melted glasses have been also recognized (e.g. Stöffler & Hornemann 1972). The formation of shock-melted glasses, characterized by closer relation of the physical properties to normal glasses quenched from melt, requires much higher shock pressures and consequently higher shock temperatures. The release adiabat for the shock-melt state must be quite different from the release adiabats discussed here. There appears to be no significant change in the unloading behaviour for quartz release paths observed up to the Hugoniot pressure of 108 GPa (Chhabildas & Miller 1985). This is consistent with the shock-temperature measurements of quartz that are required to support the presence of crystalline stishovite without melting up to a pressure of about 110 GPa (Lyzenga *et al.* 1983), although the shock equation of state for quartz at much higher pressures reveals some phase transformation (Trunin *et al.* 1970).

For anorthite glass, the adiabatic releases from Hugoniot pressures of up to 40 GPa are consistent with the frozen high- and low-pressure-phase mixture (Boslough, Ahrens & Mitchell 1986). The releases from shock pressures much higher than 90 GPa, however, showed a significant change of the release adiabat slope. It seems to be due to melting according to a proposed phase diagram for anorthite (Schmitt & Ahrens 1983). For the other feldspars, no significant change of the adiabatic release behaviour was observed, at least up to the Hugoniot pressure of 46 GPa (Ahrens *et al.* 1969b; Grady & Murri 1976). The results of investigations of post-shock samples reveal slightly lower pressure values for formation of shock-fused glasses, i.e. about 43 GPa for feldspars and 50 or 40 GPa for quartz (Stöffler & Hornemann 1972; Tattevin *et al.* 1990).

P–V–E relations for quartz and granite

The pressure–volume unloading paths depicted in Figs 6–8 provide additional information regarding energies, and hence temperatures, achieved during the shock and subsequent release process. This offers a means to test further the inferred release paths by comparing shock and post-shock temperatures with available data and theoretical expectations. The specific energy due to compression is obtained from conservation of energy across the shock front:

$$E_H = P_H(V_0 - V)/2. \quad (11)$$

The Hugoniot energies for quartz and granite are listed in Tables 6 and 7 for points in the mixed-phase region corresponding to increasing fractions of frozen high-pressure material. Integration of the P–V release paths in Figs 7 and 8 yields the total energy under the release isentrope, E_r. These are also listed in Tables 6 and 7 for quartz and granite, respectively. Residual (post-shock) temperatures were calculated from

$$T_r = T_0 + (E_H - E_r)/\bar{C}_v, \quad (12)$$

where $\bar{C}_v$ is the average specific heat at constant volume over the temperature interval $T_r - T_0$.

The resulting post-shock temperatures for quartz and granite are contained in Tables 6 and 7 and Fig. 9. For quartz, the maximum temperature achieved is 1673 K, which is less than the 1 atm melting temperature of SiO_2 (1996 K). The maximum temperature achieved in granite is similar (1713 K at 40 GPa). We therefore infer that at pressures between 15 and 40 GPa both quartz and granite remain solid upon isentropic unloading. As discussed above, Chhabildas & Miller (1985) infer that release from pressures above 50 GPa results in a high-density quartz liquid. The transition

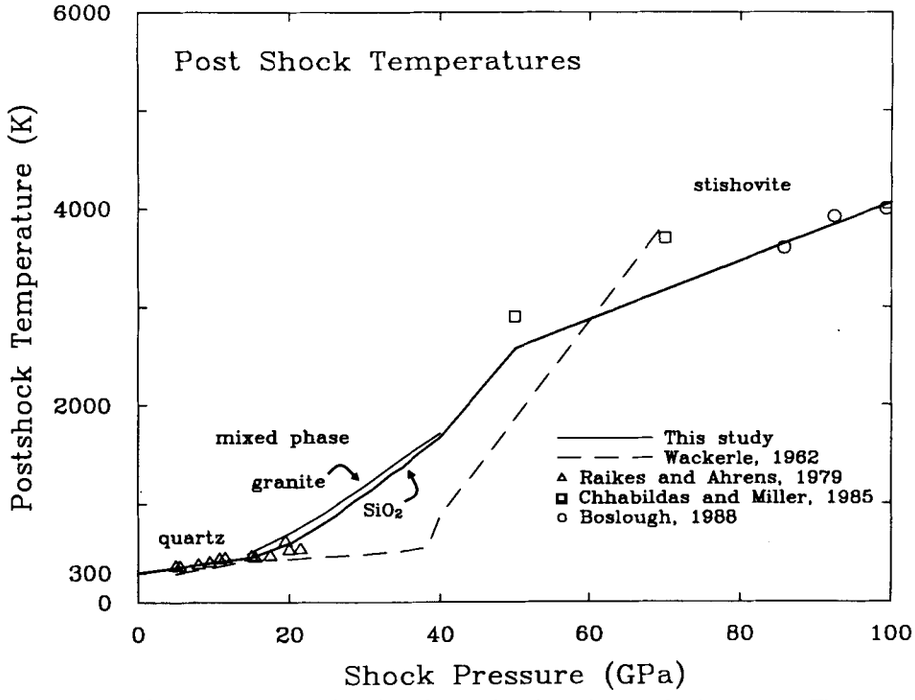

Figure 9. Post-shock temperatures for quartz and granite plotted as a function of peak shock pressure. The heavy solid line represents preferred values for post-shock temperatures in quartz between 0 and 100 GPa. Post-shock temperatures calculated for granite in the mixed-phase region are shown as the solid line. Also shown are experimental determinations for SiO_2 in both the quartz and stishovite stability fields. The data sets of Raikes & Ahrens (1979) and Boslough (1988) are from measurements of post-shock radiation. The data of Chhabildas & Miller (1985) represent calculated values determined from measured wave profiles and the Mie–Grüneisen equation. The dashed line is the calculation of Wackerle for SiO_2.

energy associated with the transformation of the high-pressure component to diaplectic glass can be estimated using the quartz-to-fused-quartz transition energy ($123\,J\,g^{-1}$) for the transforming high-pressure-phase fraction. The effect of including this term is to produce a slight change in the calculated post-shock (and shock) temperature.

Also shown in Fig. 9 are experimentally determined post-shock temperatures for quartz (Raikes & Ahrens 1979) and stishovite (Chhabildas & Miller 1985; Boslough 1988). The present results are in good agreement with the highest pressure quartz data, but are ~500 K colder than the stishovite data extrapolated to the top of the mixed-phase region (~40 GPa). The results of Chhabildas & Miller (1985), and possibly also of Boslough (1988), do not represent complete unloading and may therefore overestimate the residual temperature. The calculation of Wackerle (1962) based on the Mie–Grüneisen Equation predicts lower temperatures in the mixed-phase region and a P–T slope in the stishovite field that is much steeper than that suggested by the experiments.

The temperature decrease along the isentropic path from the shock state to complete unloading can be used to infer the Hugoniot temperature. Using the definition of the Grüneisen parameter, together with the assumption that γ/V is constant, results in the following:

$$T_H = T_r \exp\left[\frac{\gamma_0}{V_0}(V_r - V_H)\right], \tag{13}$$

where the subscript 'H' refers to Hugoniot conditions, 0 to the initial state, and 'r' to the post-shock state. Hugoniot temperatures calculated in this manner are displayed in Tables 6 and 7 and Figs 10 and 11. The incorporation of the quartz–fused-quartz phase transition energy has only a small effect (Fig. 10). Temperatures in the mixed-phase region are found to increase much more rapidly with pressure than those in either the low-pressure phase or high-pressure phase. This is due to large increases in energy caused by the large volume change associated with the transformation. It is interesting to note that the calculated temperature for SiO_2 at the top of the mixed-phase region is very similar to the extrapolated value for stishovite at that pressure based on the measurements of Lyzenga *et al.* (1983). This contrasts with the calculation of Wackerle (1962), who used a different approach for calculating the temperatures and predicted a very shallow P-T slope in the mixed-phase region, but a much steeper slope than is observed in the stishovite region. Fig. 11 demonstrates that shock temperatures for quartz and granite are very similar in the mixed-phase region. The calculated temperature for granite at the top of the mixed-phase region is ~700 K higher than that calculated for the high-pressure phase at nearly the same pressure. This difference may reflect uncertainties in the properties of the high-pressure phase. Temperatures for the high-pressure phase were obtained using the approach of McQueen *et al.* (1970) and the classical limit of 3R (R = gas constant) for the specific heat. These results demonstrate that the present models for both quartz and granite are generally consistent from an energetic viewpoint, and produce temperatures in reasonable accord with expected behaviour.

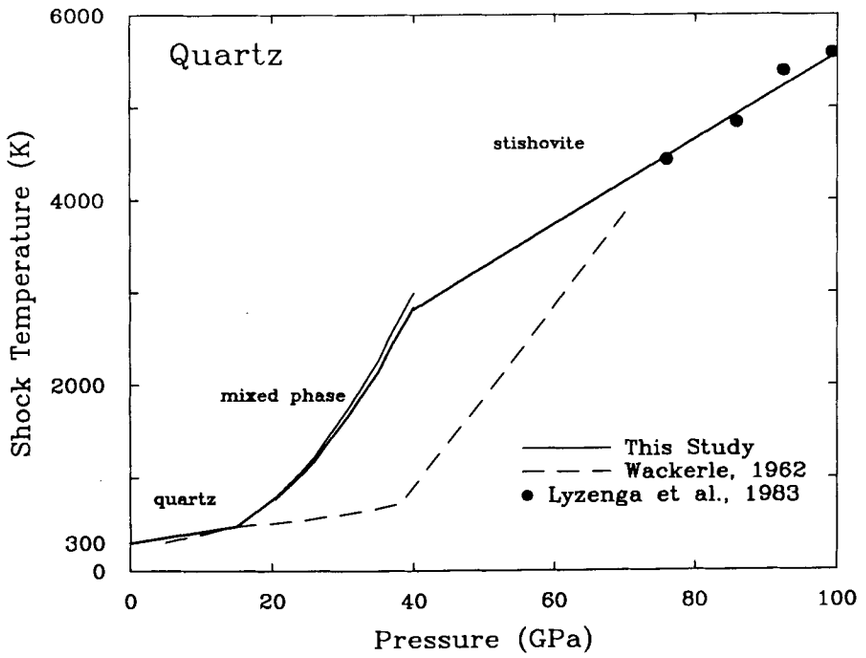

Figure 10. Shock temperatures in SiO_2 as a function of shock pressure. The heavy solid line represents preferred values of shock temperature in the low-pressure, mixed-phase, and high-pressure regimes of SiO_2. The steep P–T slope calculated for the mixed-phase region in this study contrasts with the shallow slope calculated by Wackerle (1962). The data of Lyzenga *et al.* (1983) were obtained from pyrometer measurements. The present results agree well with the extrapolated trends from this data set.

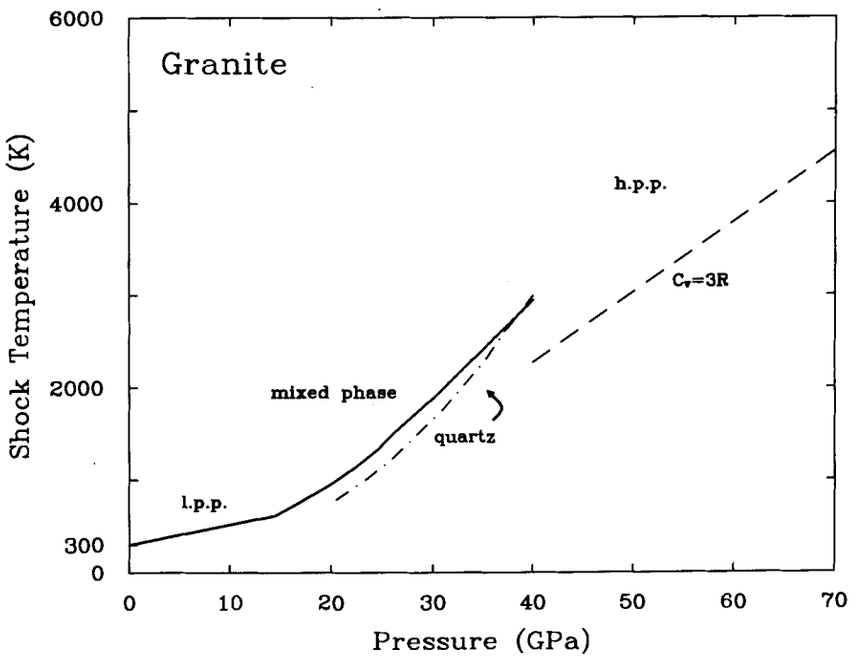

Figure 11. Shock temperatures in granite as a function of shock pressure. Preferred values of the shock temperature of granite in the low-pressure and mixed-phase regions are shown by the heavy solid line. In the mixed-phase region, granite temperatures are similar to those in SiO_2. The temperature at the top of the mixed-phase region is ~700 K higher than calculated values for the high-pressure phase of granite, assuming $\gamma_0 = 1$ and $C_v = 1.19\,J\,g^{-1}\,K^{-1}$.

CONCLUSIONS

New equation of state data for granite have been obtained and combined with the Westerly granite data of McQueen *et al.* (1967). The shock equation of state can be described by two linear relations, $U_s = 4.40 + 0.6U_p$ (km s^{-1}) for a range of U_p up to 2 km s^{-1}, and $U_s = 2.66 + 1.49U_p$ for a range of U_p from 2 to 5 km s^{-1}. These shock equations of state are comparable with other data previously determined for various granites. The third-order Birch–Murnaghan equation of state parameters are $K_{os} = 51$–57 GPa and $K'_{os} = 1.4$–1.8 for the low-pressure regime ($\rho_0 = 2.63$ g cm^{-3}), and $K_{os} = 251 \pm 30$ GPa for an assumed $K'_{os} = 4$ for the high-pressure regime ($\rho_0 = 4.02$ g cm^{-3}). These parameters are comparable to those of quartz and feldspar in the low-pressure regime, and those of stishovite and the hollandite form in the high-pressure regime.

The compressive wave structure of dry and water-saturated granite at 10–15 GPa can be described by a rate-dependent stress relaxation material model. There are significant differences in the loading wave structures of dry and water-saturated granite. The effect of water saturation is to decrease the yield strength by ~25 per cent and to increase the material relaxation time by ~75 per cent.

For the release adiabats from the mixed-phase regime, the mixed Hugoniot model is applied and compared with experimental data. In this model, the release adiabats are: calculated for the high-pressure-phase and low-pressure-phase mixture, with the same mass fraction as at the Hugoniot state, to critical pressures given by P(GPa) = 29.1–77.2 V (cm^{-3} g^{-1}). Further releases below the critical pressures are associated with large volume changes related to the formation of diaplectic glasses as quenched modifications of the high-pressure fractions.

Based on the measurements of partially released states of granite, as well as quartz shocked in the high-pressure regime ($P > 50$ GPa), it is proposed that the high-pressure form relaxes isentropically to a metastable, intermediate phase characterized by dense, highly disordered material. This material is subsequently quenched to diaplectic glass. The process of diaplectic glass formation differs from that of shock-fused glass, which can result only from a much higher Hugoniot pressure. The release adiabat associated with the shock-fused glass formation must be distinguished from the release adiabat discussed in the present study. The inferred release curves from the mixed region for quartz yield Hugoniot temperatures that are considerably higher than those of Wackerle (1962), but are consistent with the data of Lyzenga *et al.* (1983). Moreover, the post-shock temperatures predicted agree closely with the data of Raikes & Ahrens (1979) at low pressures and the data of Chhabildas & Miller (1985) and Boslough (1988) at higher pressures. These agreements lend further support to the release model developed here.

ACKNOWLEDGMENTS

We are grateful to Michael Long and Epaprodito Gelle for their assistance in maintaining the guns and preparing samples. The helpful comments proffered by S. Peyton are appreciated. John Beckett helped us to make granite glass for probe analysis. The research was supported under AFGL and Mission Research Corporation Contracts GL F19627-88-K-0034 and SC-0064-90-0002, respectively. Contribution number 5004, Division of Geological and Planetary Sciences.

REFERENCES

Ahrens, T.J., 1987. Shock wave techniques for geophysics and planetary physics, in *Methods of Experimental Physics,* **24,** pp. 185–235, eds Sammis, C.G. & Henyey, T.L., Academic, San Diego, CA.

Ahrens, T.J. & Rosenberg, J.T., 1968. Shock metamorphism: Experiments on quartz and plagioclase, in *Shock Metamorphism of Natural Materials,* pp. 59–81, eds French, B.M. & Short, N.M., Mono Book Corp., Baltimore.

Ahrens, T.J. & Jeanloz, R., 1987. Pyrite: Shock compression, isentropic release, and composition of the Earth's core, *J. geophys. Res.,* **92,** 10 363–10 375.

Ahrens, T.J., Andersen, D.L. & Ringwood, A.E., 1969a. Equation of state and crystal structures of high-pressure phases of shocked silicates and oxides, *Rev. Geophys.,* **7,** 667–707.

Ahrens, T.J., Peterson, C.F. & Rosenberg, J.T., 1969b. Shock compression of feldspars, *J. geophys. Res.,* **74,** 2727–2746.

Alt'shuler, L.V. & Sharipdzhanov, I.L., 1971. Additive equations of state of silicates at high pressures, *Izv. Earth Phys.,* **3,** 11–28 (in English).

Angel, R.J., Hazen, R.M., McCormick, T.C., Prewitt, C.T. & Smyth, J.R., 1988. Comparative compressibility of end-member feldspars, *Phys. Chem. Minerals,* **15,** 313–318.

Barker, L.M. & Hollenbach, R.E., 1972. Laser interferometer for measuring high velocities of any reflecting surface, *J. appl. Phys.,* **43,** 4669–4675.

Birch, F., 1961. The velocity of compressional waves in rocks to 10 kilobars 2, *J. geophys. Res.,* **66,** 2199–2224.

Boslough, M., 1988. Postshock temperatures in silica, *J. geophys. Res.,* **93,** 6477–6484.

Boslough, M.B., Ahrens, T.J. & Mitchell, A.C., 1986. Shock temperatures in anorthite glass, *Geophys. J.R. astr. Soc.,* **84,** 475–489.

Chhabildas, L.C. & Grady, D.E., 1984. Dynamic material response of quartz at high strain rates, in *Mat. Res. Soc. Symp. Proc.,* vol. 22, pp. 147–150, Elsevier Science Publ. Co., New York.

Chhabildas, L.C. & Miller, J.M., 1985. *Release-adiabat measurements in crystalline quartz,* Rep. SAND 85-1092, Sandia National Laboratory, Albuquerque, NM.

DeCarli, P.S. & Jamieson, J.C., 1959. Formation of an amorphous form of quartz under shock conditions, *J. Chem. Phys.,* **31,** 1675–1676.

Grady, D.E. & Murri, W.J., 1976. Dynamic unloading in shock compressed feldspar, *Geophys. Res. Lett.,* **3,** 472–474.

Grady, D.E., Murri, W.J. & Fowles, G.R., 1974. Quartz to stishovite: Wave propagation in the mixed phase region, *J. geophys. Res.,* **79,** 332–338.

Grady, D.E., Murri, W.I. & DeCarli, P.S., 1975. Hugoniot sound velocities and phase transformation in two silicates, *J. geophys. Res.,* **80,** 4857–4861.

Heinz, D.L. & Jeanloz, R., 1984. The equation of state of the gold calibration standard, *J. appl. Phys.,* **55,** 885–893.

Hemley, R.J., Jephcoat, A.P., Mao, H.K., Ming, M.C. & Manghnani, M.H., 1988. Pressure induced amorphization of crystalline silica, *Nature,* **334,** 52–54.

Hemsing, W., 1979. Velocity sensing interferometer (VISAR) modification, *Rev. Sci. Instrum.,* **50,** 73–78.

Heyman, D. & Hörz, F., 1990. Raman spectroscopy and X-ray diffractometer studies of experimentally produced diaplectic feldspar glass, *Phys. Chem. Miner.,* **17,** 38–44.

Huffman, A.R., Brown, J.M., Carter, N.L. & Reinold, W.U., 1993.

The microstructural response of quartz and feldspar under shock loading at variable temperatures, *J. geophys. Res.*, **98,** 22 171–22 198.

Kipp, M.E. & Lawrence, R.J., 1982. *WONDY V—A one-dimensional finite-difference propagation code,* Rep. SAND 81-0930, Sandia National Laboratories, Albuquerque, N.M.

Kleeman, J.D., 1971. Formation of diaplectic glass by experimental shock loading of orthoclase, *J. geophys. Res.*, **76,** 5499–5503.

Kleeman, J.D. & Ahrens, T.J., 1973. Shock-induced transition of quartz to stishovite, *J. geophys. Res.*, **78,** 5954–5960.

Lyzenga, G.A., Ahrens, T.J. & Mitchell, A.C., 1983. Shock temperatures of SiO_2 and their geophysical implications, *J. geophys. Res.*, **88,** 2431–2444.

Marsh, S.P., 1980. *LASL Shock Hugoniot Data,* University of California Press, Berkeley, CA.

McQueen, R.G., Fritz, J.N. & Marsh, S.P., 1963. On the equation of state of stishovite, *J. geophys. Res.*, **68,** 2319–2322.

McQueen, R.J., Marsh, S.P. & Fritz, J.N., 1967. Hugoniot equation of state of twelve rocks, *J. geophys. Res.*, **72,** 4999–5036.

McQueen, R.G., Marsh, S.P., Taylor, J.W., Fritz, J.N. & Crater, W.J., 1970. The equation of state of solids from shock wave studies, in *High-Velocity Impact Phenomena,* pp. 249–419, ed. Kinslow, R., Academic Press, San Diego.

Milton, D.J. & DeCarli, P.S., 1963. Maskelynite: Formation by explosive shock, *Science,* **140,** 670–671.

Nur, A. & Simmons, G., 1969. The effect of viscosity of a fluid phase on velocity in low porosity rocks, *Earth planet. Sci. Lett.*, **7,** 99–108.

Podurets, M.A., Simakov, G.V. & Trunin, R.F., 1976. On the phase equilibrium in shock-compressed quartz and the kinetics of phase transitions, *Phys. Solid Earth,* **12,** 419–424.

Raikes, S.A. & Ahrens, T.J., 1979. Post-shock temperatures of minerals, *Geophys. J. R. astr. Soc.*, **58,** 717–748.

Rice, M.H., McQueen, R.G. & Walsh, J.M., 1958. Compression of solids by strong shock waves, *Solid State Phys.*, **6,** 1–63.

Schmitt, D.R. & Ahrens, T.J., 1983. Temperatures of shock-induced shear instabilities and their relationship to fusion curves, *Geophys. Res. Lett.*, **10,** 1077–1080.

Sekine, T. & Ahrens, T.J., 1992. Shock-induced transformation in the system $NaAlSiO_4$–SiO_2: A new interpretation, *Phys. Chem. Miner.*, **18,** 359–364.

Sekine, T., Rubin, A.M. & Ahrens, T.J., 1991. Shock wave equation of state of muscovite, *J. geophys. Res.*, **96,** 19 675–19 680.

Simakov, G.V., Pavlovskiy, N.M., Kalashnikov, N.G. & Trunin, R.F., 1974. Shock compressibility of twelve minerals, *Izv. Phys. Solid Earth,* **8,** 488–492.

Stöffler, D. & Hornemann, U., 1972. Quartz and feldspar glasses produced by natural and experimental shock, *Meteoritics,* **7,** 371–394.

Sumino, Y. & Anderson, O.L., 1984. Elastic constants of minerals, in *Handbook of Physical Properties of Rocks,* vol. 3, pp. 39–137, ed. Carmichael, R.S., CRC Press, Boca Raton, FL.

Swegle, J.W., 1989. Irreversible phase transitions and wave propagation in silicate geologic materials, Rep. SAND 89-1443, Sandia National Laboratories, Albuquerque, NM.

Swegle, J.W., 1990. Irreversible phase transition and wave propagation in silicate materials, *J. appl. Phys.*, **68,** 1563–1579.

Tan, H. & Ahrens, T.J., 1990. Shock-induced polymorphic transition in quartz, carbon, and boron nitride, *J. appl. Phys.*, **67,** 217–224.

Tattevin, H., Syono, Y., Kikuchi, M., Kusaba, K. & Velde, B., 1990. Shock deformation of alpha quartz: Laboratory experiments and TEM investigation, *Eur. J. Mineral.*, **2,** 227–234.

Telegin, G.S., Antoshev, V.G., Bugayeva, V.A., Simakov, G.V. & Trunin, R.F., 1980. Calculated determination of Hugoniot curves of rocks and minerals, *Izv. Earth Phys.*, **16,** 319–324 (in English).

Trunin, R.F., 1986. Compressibility of various substances at high shock pressures: An overview, *Izv. Earth Phys.*, **22,** 103–114.

Trunin, R.F., Simakov, G.V., Podurets, M.A., Moiseyev, B.N. & Popov, L.V., 1970. Dynamic compressibility of quartz and quartzite at high pressure, *Izv. Earth Phys.*, **1,** 3–12.

Trunin, R.F., Simakov, G.V., Dudoladov, I.P., Telegin, G.S. & Trusov, I.P., 1988. Rock compressibility in shock waves, *Izv. Earth Physics,* **24,** 38–42.

Van Thiel, M., 1977. Compendium of Shock Wave Data, Rep. UCRL-50108, Lawrence Livermore Laboratory, Livermore, CA.

Velde, B., Syono, Y., Kikuchi, M. & Boyer, H., 1989. Raman microprobe study of synthetic diaplectic plagioclase feldspars, *Phys. Chem. Miner.*, **16,** 436–441.

Wackerle, J., 1962. Shock-wave compression of quartz, *J. appl. Phys.*, **33,** 922–937.

Williams, Q. & Jeanloz, R., 1989. Static amorphization of anorthite at 300K and comparison with diaplectic glass, *Nature,* **338,** 413–415.

Williams, Q., Knittle, E., Reichlein, R., Martin, S. & Jeanloz, R., 1990. Structural and electrical properties of Fe_2SiO_4–fayalite at ultrahigh pressures: Amorphization and gap closure, *J. geophys. Res.*, **95,** 21 549–21 563.